1 Substantially positive contributions of new particle formation to Cloud Condensation

2 Nuclei under low supersaturation in China based on numerical model improvements

3

4 Chupeng Zhang[1#], Shangfei Hai[2,11#], Yang Gao[1*], Yuhang Wang[3*], Shaoqing Zhang[4,2],

5 Lifang Sheng[2], Bin Zhao[5], Shuxiao Wang[5], Jingkun Jiang[5], Xin Huang[6], Shen Xiaojing[7],

6 Sun Junying[7], Aura Lupascu[8]，Manish Shrivastava[9], Jerome D. Fast[9], Wenxuan

7 Cheng[1], Xiuwen Guo[1], Ming Chu[1], Nan Ma[10], Juan Hong[10], Qiaoqiao Wang[10],

8 Xiaohong Yao[1] and Huiwang Gao[1]

9

10 [1]Frontiers Science Center for Deep Ocean Multispheres and Earth System, and Key Laboratory of

11 Marine Environmental Science and Ecology, Ministry of Education, Ocean University of China,

12 and Laoshan Laboratory, Qingdao, 266100, China

13 [2]College of Oceanic and Atmospheric Sciences, Ocean University of China, Qingdao, 266100,

14 China

15 [3]School of Earth and Atmospheric Sciences, Georgia Institute of Technology, Atlanta, GA, 30332,

16 USA

17 [4]Frontiers Science Center for Deep Ocean Multispheres and Earth System, and Key Laboratory of

18 Physical Oceanography, Ocean University of China, and Laoshan Laboratory, Qingdao, 266100,

19 China

20 [5]State Key Joint Laboratory of Environment Simulation and Pollution Control, School of

21 Environment, Tsinghua University, Beijing, 100084 China， and State Environmental Protection

22 Key Laboratory of Sources and Control of Air Pollution Complex, Beijing 100084, China

23 [6]School of Atmospheric Sciences, Nanjing University, Nanjing, 210023, China

24 [7]State Key Laboratory of Severe Weather & Key Laboratory of Atmospheric Chemistry of CMA,

25 Chinese Academy of Meteorological Sciences, Beijing, 100081, China

26 [8]Institute for Advanced Sustainability Studies, Potsdam D-14467, Germany

27 [9]Atmospheric Sciences and Global Change Division, Pacific Northwest National Laboratory,

28 Richland, WA, 99354, USA

29 [10]Institute for Environmental and Climate Research, Jinan University, Guangzhou, 510000, China

30 [11]CMA Earth System Modeling and Prediction Center, China Meteorological Administration,

31 Beijing 100081, China

32   [#]Authors contributed equally to this study.

33   [*]To whom correspondence to: yanggao@ouc.edu.cn, yuhang.wang@eas.gatech.edu

34

35

Abstract

New particle formation (NPF) and subsequent particle growth are important sources of condensation nuclei (CN) and cloud condensation nuclei (CCN). While many observations have shown positive contributions of NPF to CCN at low supersaturation, negative NPF contributions were often simulated in polluted environments. Using the observations in a coastal city of Qingdao, Beijing and Gucheng in North China, we thoroughly evaluate the simulated number concentrations of CN and CCN using a NPF-explicit parameterization embedded in WRF-Chem model. For CN, the initial simulation shows large biases of particle number concentrations at 10–40 nm and 40–100 nm. By adjusting the process of gas-particle partitioning, including the mass accommodation coefficient of sulfuric acid, the phase changes of primary organic aerosol emissions and the condensational amount of nitric acid, the improvement of the particle growth process yields a substantially reduced overestimates of CN. Regarding CCN, SOA formed from the oxidation of semi-volatile and intermediate volatility organic vapors (SI-SOA) yield is an important contributor. At default settings, the SI-SOA yield is too high without considering the differences in precursor oxidation rates. Lowering the SI-SOA yield under linear-H_2SO_4 nucleation scheme results in much improved CCN simulations compared to observations. On the basis of the bias-corrected model, we find substantially positive contributions of NPF to CCN at low supersaturation (~0.2%) over the broad areas of China, primarily due to competing effects of increasing particle hygroscopicity, a result of reductions in SI-SOA amount, surpassing that of particle size decreases. The bias-corrected model is robustly applicable to other schemes, such as quadratic-H_2SO_4 nucleation scheme, in terms of CN and CCN, though the dependence of CCN on SI-SOA yield is diminished likely due to changes in particle composition. This study highlights the potentially much larger NPF contributions to CCN on a regional and even global basis.

1. Introduction

New particle formation (NPF) is a process in which gaseous vapors nucleate and form critical molecular clusters, followed by subsequent growth to larger sizes through condensation and coagulation (Kulmala et al., 2004; Kulmala et al., 2013; Lee et al., 2019). Newly formed particles could effectively grow into the size of cloud condensation nuclei (CCN) under certain supersaturation (SS), which exerts an impact on the cloud microphysical process and global radiation balance (Merikanto et al., 2009; Gordon et al., 2017; Kerminen et al., 2018; Ren et al., 2021). In addition, the efficient nucleation and explosive growth of particles may contribute to the formation of haze (Guo et al., 2014), affecting air quality and human health (Yuan et al., 2015; Chu et al., 2019; Kulmala et al., 2021).

The overestimate of condensation nuclei (CN) in numerical models is commonly seen, despite the attempt to rectify the bias (Matsui et al., 2013; Arghavani et al., 2022). It is a common way to reduce the nucleation rate which may reduce the particle number concentration in proportion (Matsui et al., 2013). For instance, in the study of NPF in East Asia in the spring of 2009, even after lowering the nucleation rate in a regional model of WRF-Chem applied in their study, the reduced number concentration of particles at 10–130 nm remained to be overestimated (Matsui et al., 2013). Using the same regional model and a similar method to reduce the nucleation rate, Arghavani et al. (2022) found particle number concentration at 10–100 nm was still overestimated by nearly one order of magnitude, despite the effectiveness to reduce the overestimates for the smaller particles such as 2.5–10 nm. In addition to the rate of NPF, the growth process of particles also has a crucial effect on particle number concentration and size distribution. In this process, the condensation of some chemical species such as sulfuric acid, nitrate and organic gases on particles plays a major role in particle growth (Yao et al., 2018; Lee et al., 2019; Li et al., 2022), and the uncertainty of their condensation amount may lead to the bias of CN simulation.

In addition to CN, there are large discrepancies in the predicted CCN between the numerical models and observational results. Furthermore, as an important source of CCN (Merikanto et al., 2009), the contribution of nucleation to CCN quantified by

96   numerical models is also highly uncertain. For example, in terms of predicting CCN,

97   Fanourgakis et al. (2019) evaluated the CCN concentrations simulated by 16 global

98   aerosol–climate and chemistry transport models with observations at 9 sites in Europe

99   and Japan from 2011 to 2015, and found that all models underestimated CCN

100   concentrations with a mean normalized mean bias of -36% at low supersaturation

101   (SS=0.2%). WRF-Chem models also tend to underestimate the contribution of NPF on

102   CCN, especially at low supersaturation. The continuous observation of CCN

103   concentrations throughout the year (July 2008–June 2009) carried out in Hyytiälä,

104   Finland, showed that under low SS, nucleation enhanced the CCN by 106% and 110%

105   at SS=0.1% and 0.2% respectively (Sihto et al., 2011). Observations acquired in Beijing

106   from July 12 to September 25, 2008, also suggested that nucleation significantly

107   increases CCN at all supersaturations, even when supersaturation is low (i.e., 0.07%

108   and 0.26%). Thus, the occurrence of NPF enhanced CCN by a factor of 1.7 and 2.2,

109   respectively (Yue et al., 2011).

110   However, previous numerical experiments behave oppositely. For instance, Matsui

111   et al. (2011) quantified the contribution of nucleation to CCN using WRF-chem in

112   Beijing in August and September 2006 and found reduced CCN under low SS, e.g.,

113   when SS=0.02%, the concentration of CCN is reduced by up to ~50%. They attributed

114   this to the fact that the small particles produced by nucleation may inhibit the growth

115   of the preexisting particles (Matsui et al., 2011). Similarly, Dong et al. (2019) conducted

116   NPF simulations with the WRF-Chem for the summer of 2008 focusing on the Midwest

117   of the United States, and found that the nucleation resulted in decreased CCN at low

118   supersaturation (SS=0.1%). Besides, a study carried out for East Asia in 2009 also

119   indicated that at low supersaturation (e.g. SS=0.1%), nucleation has little impact on

120   CCN (Matsui et al., 2013). The contrasting effects of nucleation on CCN at low

121   supersaturations in model and observations is not explained in these previous studies.

122   At the stage of particle growth, secondary organic aerosol (SOA) formed by

123   atmospheric oxidation of organic vapors is a major contributor to particle growth to

124   CCN-related sizes (Liu and Matsui, 2022; Qiao et al., 2021). SOA formed by multi-

125   generational gas-phase oxidation of semi-volatile and intermediate volatility organic

compounds (S/IVOC) is called SI-SOA (Jimenez et al., 2009; Zhang et al., 2007). Zhao et al. (2016) made a comprehensive assessment of the roles of various SOA precursors in SOA formation in real atmosphere in China in 2010, and the results demonstrated that evaporated POA and IVOC (i.e. S/IVOC) made a significant contribution to SOA, contributing up to 82% to the average SOA concentration in eastern China. However, the effect of SI-SOA on CCN has not been fully studied.

In this paper, WRF-Chem was applied to simulate the effect of the NPF on CCN in China in February 2017. The simulated results from the WRF-Chem model are firstly compared with observations in Qingdao, Beijing and Gucheng, exhibiting large biases in CN. This is followed by an improvement through a few processes. At the end, the impact of SI-SOA yield and nucleation on CCN is investigated.

2. Data and methods

2.1 Observations

The measurements used in this study were carried out over the sampling site from February 5 to 24, 2017 at the campus of Ocean University of China (36°09′37″N, 120°29′44″E) in Qingdao, which is surrounded by residential buildings and is situated about 10 km away from the city center. A fast mobility particle sizer (FMPS, TSI Model 3091) was applied to measure the aerosol particle size distribution for the size range of 5.6 nm to 560 nm (Liu et al., 2014b). The bulk CCN concentration is measured by a cloud condensation nuclei counter at three different supersaturations (0.2%, 0.4% and 0.6%) and each supersaturation lasts for 20 minutes. More information about the CCN measurement can be found in Li et al. (2015). The urban site in Beijing is located on the roof of the building of the Chinese Academy of Meteorological Sciences (CAMS, 39°95′N, 116°33′E) in the campus of the China Meteorological Administration, close to the main road with heavy traffic. The rural site is Gucheng (GC, 39°08′N, 115°40′E), located in Hebei Province, surrounded by farmland, and is a representative station of the severity of air pollution in Beijing Tianjin Hebei region. The particle number size distribution of these two sites in the range of 4–850 nm is measured by a Tandem Scanning Mobility Particle Sizer (TSMPS), and more information about the instruments can be found in Shen et al. (2018).

2.2 Model configurations

WRF-Chem version 3.9 is used to simulate NPF events, with the main physical and chemical parameterization settings summarized in Table 1. The spatial resolution is 36 km by 36 km with 35 vertical layers and a model top at 50 hPa. The regional model simulations at a higher spatial resolution may be desirable in future when urban pollution is focused. A continuous run from February 1 to 25, 2017, was conducted, with the first five-day results as the spin-up and discarded in the analysis.

Table 1 WRF-Chem model configurations used in this work

	Model configuration
Microphysics	Morrison 2-moment microphysics scheme (Morrison et al., 2009)
Planetary Boundary Layer (PBL)	YSU boundary layer scheme (Hong et al., 2006)
Longwave and Shortwave Radiation	RRTMG longwave and shortwave radiation (Iacono et al., 2008)
Land model	Unified Noah Land Surface scheme (Chen and Dudhia, 2000; Tewari et al., 2016)
Cumulus	Grell-3D cumulus parameterization scheme (Grell, 1993)
Aerosol module	MOSAIC module (Zaveri et al., 2008; Matsui et al., 2011)
Gas-phase Chemistry	SAPRC-99 gas-phase chemistry scheme (Carter, 2000)

The meteorological initial and boundary conditions are driven by Climate Forecast System model version 2 (CFSv2; (Saha et al., 2014)) reanalysis developed by National Centre for Environmental Prediction (NCEP). The initial and boundary chemical conditions of WRF-Chem are provided by Community Atmosphere Model with Chemistry (CAM-Chem; (Buchholz et al., 2019)). Anthropogenic emissions for the year of 2017 are obtained from the Multiresolution Emission Inventory for China (MEIC, http://www.meicmodel.org/) emission dataset (Li et al., 2017; Zheng et al., 2018).

The Model for Simulating Aerosol Interactions and Chemistry (MOSAIC) was used to delineate dynamic gas-particle mass transfer to represent the condensation growth of aerosol (Zaveri et al., 2008). The gas-particle partitioning of gas species on particles is regulated by the mass transfer rate, which is related to mass accommodation coefficient (α), a parameter involved in the model representing the probability of gas molecules entering the bulk liquid phase (Pöschl et al., 1998). The original setting of α for all condensing species for all size bins a in MOSAIC is 0.1 (Zaveri et al., 2008). In the default release of WRF-Chem, MOSAIC was implemented in the sectional framework with aerosol size distributions divided into 4 or 8 size bins spanning 39 nm to 10 μm in diameter. To explicitly express the nucleation and the growth of newly formed particles, the aerosol size range in the MOSAIC module was extended from 1 nm to 10 μm, with the number of aerosol size bins increased to 20 (Matsui et al., 2011; Matsui et al., 2013; Lupascu et al., 2015; Lai et al., 2022). The calculation method of CCN concentration in the WRF-chem model is referred to the study of Matsui et al. (2011). Based on Köhler theory, CCN concentrations under the three given supersaturations of 0.2%, 0.4% and 0.6% were calculated. The critical supersaturation (S_c) of each size bin in the WRF-chem model was calculated by the following formula:

$$S_c = \sqrt{\frac{4 \times a^3}{27 \times r^3 \times \kappa}} \tag{1}$$

$$a = \frac{2 \times \sigma}{R_v \times T \times \rho_\omega} \tag{2}$$

Where α (m) is the coefficient of the Kelvin effect, κ is the volume−averaged hygroscopicity, calculated using these values in Table 1, r (m) is the dry diameter, σ is droplet surface tension over water (0.076 N m^{-1}), R_v is the gas constant for water vapor (461.6 J K^{-1}kg^{-1}), T (K) is the air temperature, and ρ_ω is the density of water (1000 kg m^{-3}).

Table 2 Hygroscopicity Parameters (κ) in the WRF-Chem Model

Species	Hygroscopicity (κ)
Sulfate	0.5
Ammonium	0.5
Nitrate	0.5
Black carbon	10^{-6}
Primary organic aerosol	0.14
Other inorganics	0.14
Sodium	1.16
Chloride	1.16

The chemical aging process of organic aerosols (OA) is modeled by the volatility basis set (VBS) approach, which was widely used in air quality models to represent complex mixtures of thousands of organic species (Donahue et al., 2006; Shrivastava et al., 2011; Chrit et al., 2018). The VBS method classifies compounds according to the effective saturation concentration (c^*), which represents the proportion of the component in the gas phase to the particle phase (Donahue et al., 2006), and species with higher c^* values are more volatile. The oxidation of highly volatile precursors to form relatively low volatile components represents the aging process of OA. OA consists of directly emitted primary organic aerosols and photochemically produced secondary organic aerosols (SOA) (Shrivastava et al., 2011). In this study, the simplified 2-species VBS mechanism was applied to the simulation of SOA, during which primary organic aerosol was represented by two species based on volatility with effective saturation concentration c^* values (at 298 K and 1 atm) of 10^{-2} and 10^5 µg m^{-3} (Shrivastava et al., 2011). Primary organic aerosols with c^* of 10^5 µg m^{-3} refers to S/IVOC, which is in the gas phase under most atmospheric conditions due to its high volatility, while for those primary organic matters with c^* of 10^{-2} µg m^{-3}, is treated as gas phase as well in the original model. The SOA formed by photochemical oxidation of S/IVOC precursors is called SI-SOA and the SOA formed by oxidation of VOC precursors is named V-SOA. In the simplified 2-species VBS mechanism, SI-SOA (c^*

of 10^{-2} μg m^{-3}) is formed by the oxidation reaction of S/IVOC precursors ($c*$ of 10^5 μg

m^{-3}) and OH with an oxidation rate constant of 4×10^{-11} cm^3 molec^{-1} s^{-1}. The equations

for controlling the oxidation of S/IVOC precursors are as follows:

$$POA(g)_{e,c} + OH \rightarrow SI - SOA(g)_{e,c} + 0.15SI - SOA(g)_{e,o} \tag{3}$$

$$POA(g)_{e,o} + OH \rightarrow SI - SOA(g)_{e,o} + OH \tag{4}$$
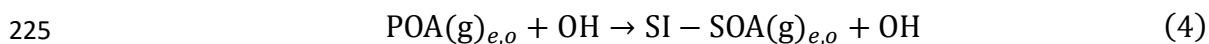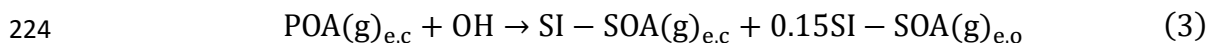
where POA(g) denotes primary organic aerosols with $c*$ of 10^5 μg m^{-3}, which reacts

with OH to form SI-SOA(g) with $c*$ of 10^{-2} μg m^{-3}. Subscripts c and o represent the

non-oxygen and oxygen parts respectively of given species and e is either the biomass

or anthropogenic emission sector. In addition, SVOC and IVOC emissions

corresponding to both anthropogenic and biomass burning emissions are derived based

on constant emission ratio of S/IVOC to POA (Shrivastava et al., 2011). A detailed

description of 2-species VBS mechanism can be found in Shrivastava et al. (2011).

2.3 Model sensitivity formulations

Three sets of sensitivity tests are designed and listed in Table3. The purposes of

the three sets of experiments are as follows: (1) Adjust the condensation growth process

of ultrafine particles in WRF-Chem model (Base, MAC, PEP, NOCD, RACD, with

details in Table 3).; (2) Explore the effect of SI-SOA yield on CCN (Low_Yield and

High_Yield); (3) Study the effect of nucleation process on CCN under the change of

SI-SOA yield (Low_Yield and High_Yield and their corresponding cases without

nucleation parameterization, i.e., Low_nucoff and High_nucoff). Each scenario will be

explained in conjunctions with the results.

Table 3 The sensitivity tests involved in this study

Purposes	Simulation scenarios	Description
Adjust the condensation growth process of ultrafine particles	Base	Simulation with the default setting with nucleation coefficient set as $2 \times 10^{-6}\,\mathrm{s}^{-1}$, the same as Lai et al. (2022)
	Mass accommodation coefficient (MAC)	It is the same as Base except that the mass adjustment coefficient (α) of gaseous sulfuric acid is adjusted from 0.1 to 0.65.
	POA emission phase (PEP)	It is the same as MAC except that the phase of POA is changed from gas phase to particle phase.
	No condensation (NOCD)	It is the same as PEP except that no NH_4NO_3 condenses on particles below 40 nm.
	Ratio method for condensation (RACD)	It is the same as PEP except that the condensation of NH_4NO_3 on particles below 40 nm is reduced according to the ratio of acid particles to total particles reported in Wang et al. (2014).
Explore the effect of SI-SOA yield on CCN (Explore the effect of nucleation process on CCN under the change of SI-SOA yield)	High_Yield	Simulation with high oxidation rate of SI-SOA formation with reaction rate constant of 5×10^{-11} $cm^3\ molec^{-1}\ s^{-1}$
	Low_Yield	Simulation with low oxidation rate of SI-SOA formation with reaction rate constant of 2×10^{-11} $cm^3\ molec^{-1}\ s^{-1}$

| Explore the effect of nucleation process on CCN under the change of SI-SOA yield | High_NUCOFF | Simulations without nucleation parameterizations based on High_Yield |
| | Low_ NUCOFF | Simulations without nucleation parameterizations based on Low_Yield |

254

3. Results

3.1 Observational analysis

Based on the criteria (Dal Maso et al., 2005; Kulmala et al., 2012), NPF is defined as an event with the emergence of a nucleation mode with particle diameters smaller than 25 nm, lasting for 2 hours or more, followed in general by a continuous particle growth. Six NPF events were identified in February 2017 in Qingdao, on the days of 6, 9, 10, 17, 20 and 23 (Fig. 1a), yielding a frequency of ~30% and displaying a typical banana-shaped growth of particles in the particle number size distribution. Compared to a few other studies on NPF frequency in Qingdao, the results in this study are to a large extent consistent with that in the fall of 2012–2013 (30%; (Zhu et al., 2019)), slightly higher than that in summer 2016 (22%; (Zhu et al., 2019)) and lower than that in spring of 2010 (41%; (Liu et al., 2014c). The higher frequency in spring in Qingdao is consistent with the observational results at different stations in the Northern Hemisphere in Nieminen et al. (2018).
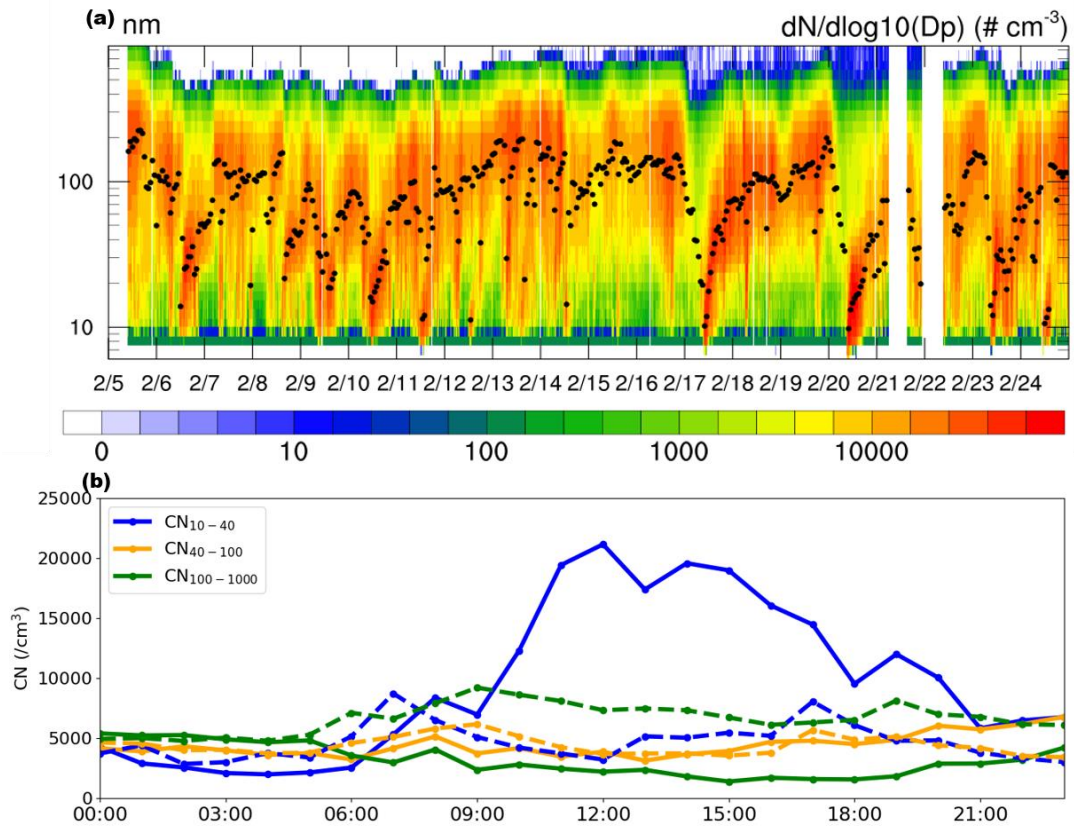
Fig. 1. Distribution of particle number concentration. (a) Temporal evolution of particle size distributions (colored shading) and geometric median diameter (GMD; dots in black) in Qingdao on February 5-24, 2017. (b) The mean diurnal variation of CN_{10-40} (blue), CN_{40-100} (orange) and $CN_{100-1000}$ (green) composited during the NPF (solid lines) and non-NPF (dashed lines) days on February 5-24, 2017. All times are local times (LT)

During the six NPF events identified in February in Qingdao, the mean diurnal cycle of CN_{10-40} (10–40 nm) particles exhibits triple peaks (solid blue in Fig. 1b), in the morning (8:00 LT), noon (12:00–14:00 LT) and evening (19:00 LT), respectively. A comparable three-peak feature was also observed in earlier years during 2016-2018 in Qingdao (Zhu et al., 2021). The morning and evening peaks of CN_{10-40}, with values of ~5300 cm^{-3} and ~12000 cm^{-3}, respectively, are likely caused by the primary emissions from traffic and cooking activities (Wu et al., 2021a; Wang et al., 2022; Cai et al., 2020). The occurrence of NPF starts approximately at 9:00 am LT, accompanied by a substantial increase in CN_{10-40} compared with non-NPF days (solid vs. dashed lines, in blue), yielding a peak around noon (20000 cm^{-3} during 12:00–14:00 LT). In addition,

286 larger particles (e.g., $CN_{40–100}$ and $CN_{100–1000}$) displayed a slow or no increase in the

287 afternoon.

288

289 **3.2 Model improvement in particle number concentration simulations**

290   Particle number concentrations, primarily in two ranges of 10–40 nm and 40–100

291 nm, are commonly simulated with large biases. In the smaller size range (10–40 nm),

292 the particle number concentration is associated with NPF and particle growth. During

293 NPF, despite differences among the formation mechanisms, H_2SO_4 is considered the

294 common species (Yu, 2005; Lovejoy et al., 2004), which often suffer large biases (Cai

295 et al., 2016; Matsui et al., 2011). In the size range of 40–100 nm, the particle number

296 concentration is primarily affected by the condensation growth of particles below 40

297 nm, which is closely related to chemical components such as SOA and nitrate. Prior to

298 the evaluation of particle number concentration, we first evaluate the compositions of

299 $PM_{2.5}$ and criteria air pollutants including $PM_{2.5}$, PM_{10}, O_3, SO_2, CO, and NO_2, showing

300 relatively low biases compared to observations (section S1 and Fig. S1 and Fig. S2 of

301 the supporting information).

302

303 **3.2.1 Bias correction of particle number concentration at 10–40 nm**

304   In this study, as shown in Fig. 2, comparisons of $CN_{10–40}$ between simulations (red

305 line in Fig. 2a) and observations (black line in Fig. 2a) results of the six NPF events

306 mentioned in the previous section in Qingdao in February 2017 indicate that model

307 overestimates $CN_{10–40}$ with mean fractional bias of 48%. As one of the major processes

308 affecting the particle number concentration of 10–40 nm, nucleation is governed by the

309 particle nucleation rate of 1 nm particles $(cm^{-3}\ s^{-1})$, which is closely associated with the

310 concentration of H_2SO_4. For instance, in a commonly applied activation mechanism,

311 the nucleation rate calculated by $J^* = K_{ACT} \times [H_2SO_4]$. Note that K_{ACT} is the nucleation

312 coefficient considering the physical properties and chemical species of nucleation

313 process under different environments, indicating that a lumped chemical species are

314 included in the scheme reflected primarily in the nucleation coefficient k, set as 2×10

315 $^{-6}\ s^{-1}$ based on previous studies (Sihto et al., 2006; Riipinen et al., 2007). Dong et al.

316 (2019) simulated NPF occurring in the summer of 2008 in the United States using the

317 NPF-explicit WRF-Chem based on the activation mechanism, which overestimated the

318 particle number concentration at 10–63 nm by nearly doubled, even when the K_{ACT}

319 decreased by one order of magnitude (set at a very low value of 10^{-7} s^{-1}). Therefore, it

320 is likely that the overestimation of particle number concentration in the smaller particle

321 size segment is probably due to the bias of simulated sulfuric acid.
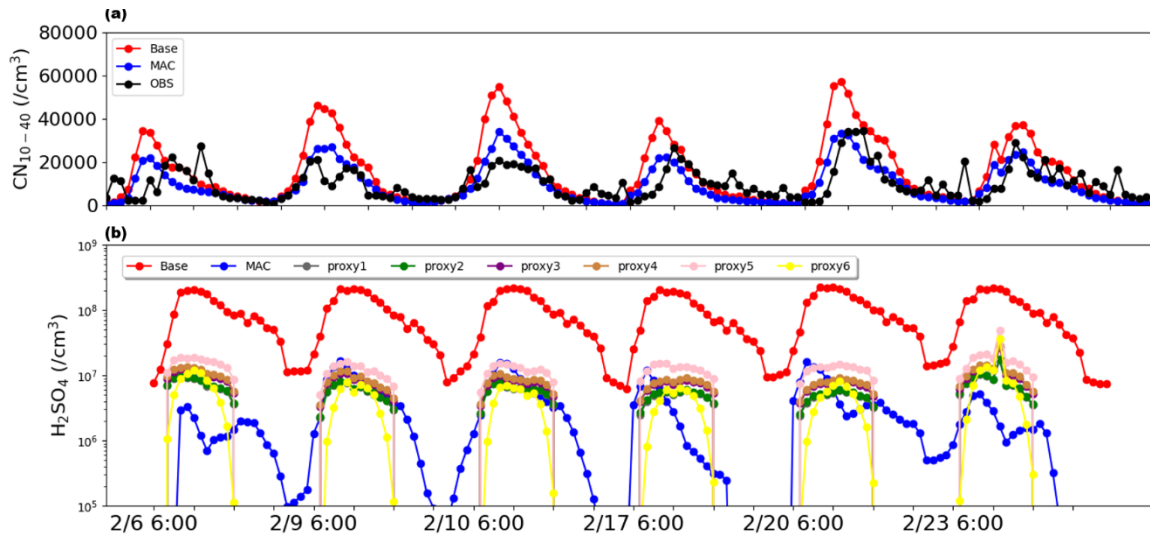
322

323 Fig. 2. Time series of (a) $CN_{10–40}$ on NPF days, where red and blue represent Base and

324 MAC simulation results respectively, and black represents observation results, and (b)

325 sulfuric acid gas concentration obtained by simulation and by proxies (dark grey: Eq.

326 5; green: Eq. 6; purple: Eq. 7; brown: Eq. 8; pink: Eq. 9; yellow: Eq. 10). All times are

327 in local times.

328

329   Measurement of sulfuric acid gases in the lower troposphere is challenging due to

330 the generally low ambient concentration of sulfuric acid (10^6–10^7 molecule cm^{-3}).

331 Different methods have been proposed to estimate ambient sulfuric acid concentrations

332 based on observations such as SO_2 (Petäjä et al., 2009; Lu et al., 2019; Mikkonen et al.,

333 2011). For instance, Petäjä et al. (2009) proposed a linear method to approximate

334 observed H_2SO_4 concentration in Hyytiälä, southern Finland. Moreover, a recent study

335 by Lu et al. (2019) proposed a nonlinear method to construct a number of proxies for

336 gaseous sulfuric acid concentration (Eq. 5–9), indicating that compared to the linear

337 method in Petäjä et al. (2009), the nonlinear relationship can provide more accurate

338 H₂SO₄ concentration in Beijing during February–March 2018 period. In addition, we

339 also used another sulfuric acid nonlinear proxy (Eq. 10) based on long-term

340 observations in Germany, Finland, the United States, etc. (Mikkonen et al., 2011). In

341 this study, we adopt the above six nonlinear proxy methods (referred as proxy5 to

342 proxy10) to estimate H₂SO₄ in Qingdao.

343
$$[H_2SO_4] = 515.74 \times [SO_2]^{0.38} \times \text{Radiation}^{0.14} \times CS^{0.03} \qquad (5)$$

344
$$[H_2SO_4] = 280.05 \cdot \text{Radiation}^{0.14}[SO_2]^{0.40} \qquad (6)$$

345
$$[H_2SO_4] = 9.95 \times [SO_2]^{0.39} \times \text{Radiation}^{0.13} \times CS^{-0.01} \times [O_3]^{0.14} \qquad (7)$$

346
$$[H_2SO_4] = 14.38 \times [SO_2]^{0.38} \times \text{Radiation}^{0.13} \times [O_3]^{0.14} \qquad (8)$$

347
$$[H_2SO_4] = 0.0013 \times [SO_2]^{0.38} \times \text{Radiation}^{0.13} \times CS^{-0.17} \times ([O_3]^{0.14} + [NO_x]^{0.41}) \quad (9)$$

348
$$[H_2SO_4] = 8.21 \times 10^{-3} \times [SO_2]^{0.62} \times \text{Radiation} \times (CS \times RH)^{-0.13} \qquad (10)$$

349 where [SO₂], [O₃] and [NOₓ] (molecule cm⁻³) represents concentration of

350 observed SO₂, O₃ and NOₓ, respectively. "Radiation" (W m⁻²) is global radiation. RH

351 (%) is the relative humidity, and CS (s⁻¹) is the condensation sink, which is calculated

352 based on observed particle distribution.

353

354 The simulated H₂SO₄ concentration from the Base simulation (dots in Fig. 2b) is

355 compared with observations obtained by proxies (see Fig. 2b), indicating that Base

356 simulations apparently overestimate by one order of magnitude compared to the H₂SO₄

357 estimated by proxies. The overestimation has been frequently reported previously, i.e.,

358 over Beijing (Matsui et al., 2011), which ascribes the bias to the overestimation of the

359 SO₂ concentration. In a more recent study, the sensitivity of H₂SO₄ to SO₂ is tested, and

360 the result shows that even when SO₂ is reduced to an unrealistically low level, the

361 simulated H₂SO₄ is still more than one order of magnitude higher than the observed

362 value (Lai et al., 2022), suggesting that the SO₂ concentration cannot fully explain the

363 overestimates.

364 In addition to the precursor of H₂SO₄, the mass accommodation coefficient (α),

365 representing the probability of impaction of a gaseous molecule on a liquid surface and

366 entering the bulk liquid phase, is another important factor affecting the concentration

of sulfuric acid gas. In the public release of WRF-Chem, mass accommodation coefficient is typically set to a low value of 0.1 for all gas species under different volatility during the condensation process, including H_2SO_4 (Davidovits et al., 2004; Zaveri et al., 2008). Recent studies indicate that the low mass accommodation coefficient value may not be applicable to the low volatile gases, which tend to have a mean mass accommodation coefficient value of 0.7 and close to the unity (Krechmer et al., 2017). In fact, an earlier study has indicated based on experimental determination, the mass accommodation coefficient of H_2SO_4 vapor in sulfuric acid aqueous solution was measured, and the best fit value was 0.65 (Pöschl et al., 1998). Accordingly, a sensitivity simulation was conducted by adjusting the mass accommodation coefficient of H_2SO_4 from 0.1 to 0.65, referred to as MAC.

This simulation brought the H_2SO_4 concentration (see Fig. 2b) much closer to the calculated results from proxies, and the corresponding biases reduced by approximately an order of magnitude. Notably, the MAC simulation decreases the overestimate of sulfuric acid gas concentration, resulting in a lower particle formation rate. The MAC simulation also significantly reduces overestimate of $CN_{10–40}$ (Fig. 2a), and mean fractional bias compared to observations decreases from 48% to 1%.

3.2.2 Improvement of particle number concentration simulations at 40–100 nm

The number concentration of particles in the 40–100 nm range is mainly affected by the coagulation and condensation processes. While the coagulation process tends to largely affect ultrafine particles below 10 nm than those with larger sizes (Wu et al., 2011), the condensation growth of particles during gas-particle partitioning at sizes of 10–40 nm, to a large extent, governs the variations in number concentration of 40–100 nm particles. The condensation process is primarily controlled by gas-particle partitioning of chemical species, which may change the chemical composition of particles, such as organic compounds and inorganics including sulfate, nitrate and ammonium.

Among the species contributing to the condensation growth of particles at 10–40 nm, the organic compounds with c^* of 10^{-2} µg m^{-3} play the dominant role (Pierce et al.,

2011). In the current model setting, the low volatile organic matter of 10^{-2} µg m^{-3} comes from two gas-phase sources, including the direct emission of primary organic aerosol (POA) and SOA formed from S/IVOC (SI-SOA), conducive to condensation on particles. While the condensation of gaseous SOA is in general reasonable, the gas phase emissions of POA may be problematic. For instance, previous studies suggested that POA is in gas phase close to the emissions source. However, with rapid dilution and cooling in the atmosphere away from the source, most POA condenses to particle-phase (Roldin et al., 2011b; Roldin et al., 2011a; Shrivastava et al., 2008). Therefore, away from the emissions source POA, being in the particle phase, will not be involved in the growth of newly formed particles. Therefore, POA may not contribute to particle growth away from the emission sources, which caused different size distributions of POA compared to when it was emitted in the gas-phase (Fig. S3a vs. Fig. S3b). Emitting low volatility POA in the particle phase eliminates the unreasonable quasi-banana shape pattern exhibiting concomitant growth of newly formed particles with increasing mass concentration of POA.

The composition analysis (Fig. S3c) in the 10–40 nm particles mass from the model results indicates that organic compounds mentioned above only account for 21% of total mass (sulfates, nitrates, ammonium salts and organics) in this size range and the dominant species is nitrate which accounts for 51% of total mass, exhibiting inconsistencies with the previous studies which in general indicates a much smaller contribution of nitrate. For instance, Liu et al. (2014a) suggested that over North China Plain in summer 2009, organic matter accounted for 77% of particles around 30 nm, while the sum of SO_4^{2-}, NO_3^- and NH_4^+ only accounted for 18%. Recent observations conducted in Beijing also indicated that particles at 8–40 nm are mainly composed of organic matter (with mass fraction of ~80%) and sulfate (with mass fraction of ~13%), while nitrate content is very low (with mass fraction of ~3%) (Li et al., 2022). Another study showed that nitrate accounted for 7–8% at urban sites and 17% at rural sites for particles mass in 7–30 nm in the United States in 2007 (Bzdek et al., 2012). Therefore, the potentially too high modeled nitrate fraction in 10–40 nm in this study is tightly associated with the condensation process, with the specific reasons explained below.

The condensation of nitric acid on particles is highly constrained by the particle acidity. The acidity in smaller particles (i.e., 10–40 nm) tends to be higher than that in large particles, primarily due to the larger condensation of H_2SO_4 (Lu et al., 2022), and particles with sizes greater than 40 nm have a much weaker acidity or are nearly neutral. For example, observed evidence has shown that acidic ultrafine particles account for a large proportion of ultrafine particles from 22 December 2010 to 15 January 2011 in Hong Kong, e.g., 65% for particles within 5.5–30 nm (Wang et al., 2014).

In the model, a particle is determined to be in solid phase when the ambient relative humidity is lower than the mutual deliquescence relative humidity of the particles (Zaveri et al., 2005; Zaveri et al., 2008), which is in general suitable for particles dominated by inorganics. In the study area, the results indicate that at most conditions relative humidity are relatively low and the particles are in solid phase, in which the condensation process is not affected by particle acidity and the condensation of nitric acid on particles is directly calculated based on the gas-particle equilibrium concentration (Zaveri et al., 2008). However, for particles below 40 nm, the main compositions are likely to be organic matter (Zhu et al., 2014; Ehn et al., 2014), which tends to be in liquid phase (Virtanen et al., 2011; Cheng et al., 2015), under which the condensation of nitric acid is strongly constrained by acidity. Therefore, the phase misrepresentation ignores the weakening effect of acidity on nitric acid condensation, resulting in too high nitrate therein.

To overcome this issue, we propose a ratio method for condensation (RACD) to partition the condensation of nitric acid on particles under 40 nm, by applying a ratio of the number concentration of non-acidic particles to ultrafine particles. The method is based on two assumptions, including: 1) little condensation of nitric acid on particles with strong acidity (Lu et al., 2022); 2) the condensation of nitric acid on particles is proportional to the ratio of the number concentration of non-acidic ultrafine particles to the total particles, despite the existence of uncertainties. Fig. S4 depicts the average particle number concentration and acid particle in the 1 to 40 nm range, calculated based on Wang et al. (2014). The ratio of non-acidic particles is 8% for particles below 10 nm, 18% for particles at 10–15.8 nm, 30% for particles at 15.8–25.1nm, and 55% for

457   particles at 25.1–39.8 nm (Fig. S4). Note that the ratio is based on measurements

458   acquired at a single site in Hong Kong, therefore more observational studies are needed

459   to warrant the robustness of the method. Alternatively, the condensation of nitric acid

460   on particles in bins from 1nm to 40 nm is completely suppressed, referred to as NOCD.

461   The simulation results based on the two methods (RACD and NOCD) are shown in

462   Fig. 3. Compared to MAC, RACD simulations reduce previously noted overestimation

463   of particle number concentration in the 40–100 nm size range (Fig. 3b), with the mean

464   fractional bias decreases from 83% to 63%. In addition to the amount of nitrate

465   condensation during particle growth mentioned above, the overestimation of particle

466   number concentrations in the 40–100 nm range may be attributed to nucleation process.

467   More specifically, in the H_2SO_4-H_2O binary nucleation mechanism used in this study,

468   when the concentration of sulfuric acid gas is reduced (Section 3.2.1), the resulting

469   decrease in nucleation rate leads to a slight decrease in particle number concentration

470   at 40–100 nm relative to Base (mean fractional bias from 98% to 83%). Apart from that,

471   it may also be related to the choice of nucleation parameterization scheme. For example,

472   using a global chemical transport model GEOS-Chem with a nucleation mechanism in

473   which formation rate is a function of the concentrations of sulfuric acid and low-

474   volatility organics, Yu et al. (2015) overestimated the concentration of particles in the

475   10–100 nm range by 161% at nine sites in the summer in North America. A possible

476   explanation for this overestimation was given by the uncertainty of the predicted

477   concentration of organic compounds involved in organics-mediated nucleation

478   parameterization. After they switched to another scheme of the ion-mediated nucleation

479   mechanism without organic matter, the number becomes 27% lower than the

480   observations (Yu et al., 2015). The test based on different schemes is beyond the scope

481   of the study, which is therefore not investigated.

482   Moreover, the overestimation of particles over 100 nm ($CN_{100–1000}$; Fig. 3c), which

483   have a strong influence on CCN, also decrease in the RACD simulation. Thus, the mean

484   fractional bias decreases from 25% (MAC) to 1%. Note that the slight increase of $CN_{10–40}$

485   through the application of RACD, can be linked to the decrease of nitrate

486   condensation, and leads to weakened particle growth and enhanced particle number

487 concentration at 10–40 nm (Fig. 3a). The alternative method by completely removing

488 the nitrate condensation (NOCD) yields even better performance in particle number

489 concentration of 40–100 nm (mean fractional bias of 34%), indicating the feasibility by

490 reducing the nitrate condensation. The proportion of nitrate simulated by RACD is 23%,

491 closer to values reported in past observations (Bzdek et al., 2011; Bzdek et al., 2012),

492 while the nitrate (1%) in the scenario of NOCD seems to be too low. Considering the

493 limited observational information obtained based on previous studies, RACD is applied

494 in this study.

495   In addition to Qingdao, we evaluate the model performance over a few other sites,

496 including one site over urban Beijing and the other one over the rural area of Gucheng,

497 yielding consistent improvements in model simulations (Section S2; Fig. S6-S8).

498 Moreover, we select another empirical scheme, e.g., kinetics, and one classical

499 nucleation scheme, indicating the empirical scheme of activation scheme is in general

500 a good option in this study (Section S2; Fig. S9-S11; Table S1-3).
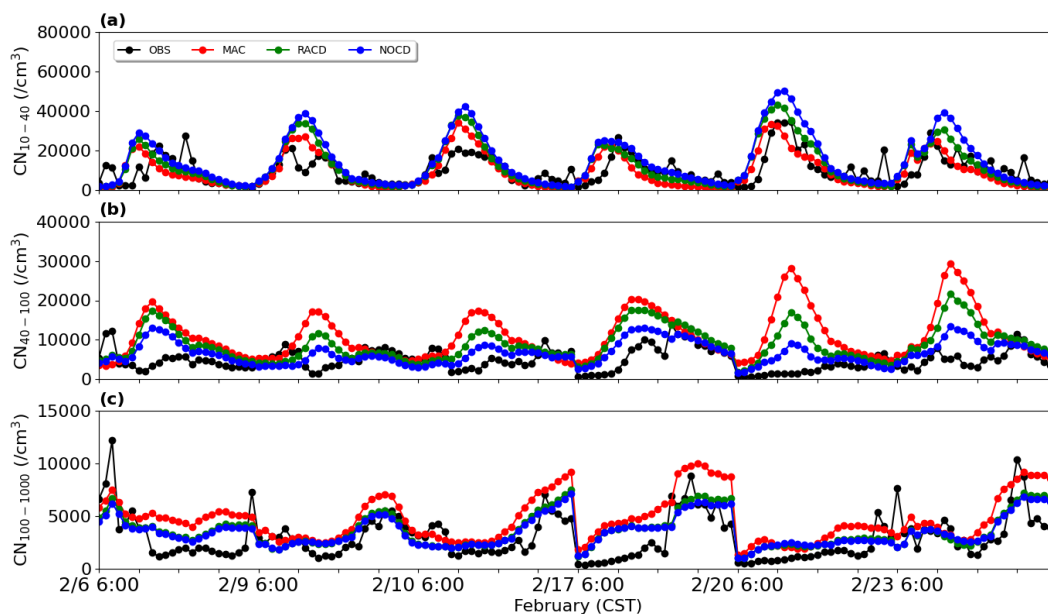
501

502 Fig. 3. The time series of (a) $CN_{10–40}$, (b) $CN_{40–100}$ and (c) $CN_{100–1000}$ on NPF days in

503 Qingdao on February 5-24 simulated from MAC (marked in red), NOCD (marked in

504 blue) and RACD (marked in green) as well as from observations (OBS) (marked in

505 black). All times are local time.

506

507

3.3 Substantial contributions of SI-SOA to CCN

Compared with the original model setting, after adjusting the growth process of ultrafine particles (RACD), the number concentration of particles tends to decrease, especially for particles above 40 nm. Ultrafine particles above 40 nm are important sources of CCN (Dusek et al., 2006), in this way, the number concentration of CCN also tends to decline. In addition, in the Base case, we found that the model overestimated $CCN_{0.4\%}$ and $CCN_{0.6\%}$, with mean fractional bias being 64% and 87%, respectively. After adjusting the condensation growth process of ultrafine particles, under high supersaturation (i.e., $CCN_{0.4\%}$ and $CCN_{0.6\%}$), the capability of the model in reproducing the CCN is improved. RACD reduces the overestimation of $CCN_{0.4\%}$ and $CCN_{0.6\%}$, with mean fractional bias reduced to 30% and 56%, respectively, although the overestimates still exist (Figs. S5b, c). However, for low supersaturation (i.e., $CCN_{0.2\%}$), the decrease of number concentration of CCN is too large, and mean fractional bias decreases from 7% to -45% (Fig. S5a), therefore the bias will be further adjusted later.

In addition to the growth process, the remaining overestimate of CCN under high SS and underestimate of CCN over low SS is likely to be influenced by the chemical compositions involved in the activation of ultrafine particles into CCN. Specifically, ultrafine particles can grow up to CCN size under certain SS (Pierce and Adams, 2007). This process is influenced by both particle size and hygroscopicity, and hygroscopicity is closely related to the chemical composition of particles (Petters and Kreidenweis, 2007). In particular, inorganic compounds generally increase particle hygroscopicity, increasing CCN. SOA has dual effects on CCN since it decreases particle hygroscopicity but also promotes growth of particles, and these two effects are competitive with each other (Wu et al., 2015; Zaveri et al., 2021). Ultrafine particles must grow to a critical size to be activated into CCN (Dusek et al., 2006). SOA act as a major contributor in promoting the condensational growth of ultrafine particles to the critical size, facilitating particles activation into CCN. In contrast, SOA tends to reduce the hygroscopicity of particles, leading to a diminished ability of activation to CCN (Wu et al., 2015). These two competing effects work together and modulate the number

537 of CCN. Moreover, considering that SI-SOA is the main SOA component on ultrafine

538 particles (Fig. S5d), the effect of SI-SOA on CCN is therefore explored in this study.

539 Considering SI-SOA is a product of S/IVOC oxidation, the oxidation rate of

540 S/IVOC is tightly associated with CCN, which likely affects the bias of CCN. In the

541 original model setup, the oxidation rate is set to be a constant of 4×10^{-11} cm^3 molec^{-1}

542 s^{-1} for all S/IVOC. However, a recent study (Wu et al., 2021b) proposed that the

543 oxidation rate can be as high as 5×10^{-11} cm^3 molec^{-1} s^{-1} such as for polycyclic aromatic

544 hydrocarbons (PAHs), close to the original model value, but can be as low as half (i.e.,

545 2×10^{-11} cm^3 molec^{-1} s^{-1}) of the original modeling setting for S/IVOC species except

546 PAHs (O-S/IVOCs). It is noteworthy that the oxidation rates of 5×10^{-11} and 2×10^{-11}

547 in general represent the upper and lower bounds (Zhao et al., 2016; Wu et al., 2021b).

548 To delve into how oxidation rates affect CCN, we set up a few numerical

549 experiments (Table 3) to investigate the response of CCN to the oxidation rate of

550 S/IVOC at three supersaturations (0.6%, 0.4%, 0.2%), including cases of High_Yield

551 and Low_Yield. As it is shown in Fig. 4, decreasing the oxidation rate (Low_Yield)

552 leads to a reduction of ~10% of CCN at high supersaturation (i.e., CCN0.6%) as

553 compared to the High_Yield simulation. This behaviour is a consequence of the

554 decrease of particle number concentrations associated with Low_Yield, particular of

555 the particles close to the critical diameter (40–100 nm). In this case, the effect of particle

556 size dominates the hygroscopicity. In contrast, at a lower supersaturation (CCN$_{0.2\%}$),

557 CCN increases by 42% when the oxidation rate is switched from a high to a low value,

558 which is due to the smaller fraction of SI-SOA contributing to particulate mass when

559 the oxidation rate is low. In this case, relative to SOA, a larger fraction of other particle

560 constituents such as inorganics, increase the volume weighted particle hygroscopicity

561 (Dusek et al., 2006) which causes the increase of CCN number. This means that the

562 effect of hygroscopicity on CCN surpasses the influence on particle size at low

563 supersaturations. This conclusion is consistent with the observation conducted by Ma

564 et al. (2016) in the North China Plain in 2013, which suggested that along with the

565 decrease of SS, the particles that can be activated to CCN is more sensitive to changes

566 of particle hygroscopicity. Similarly, based on observational data in northern China in

22

567 summer, Wang et al. (2023) found that CN in 2020 is lower than that in 2014 due to

568 particulate pollution control, however, the particles become more easily activated,

569 attributable to the larger extent of decrease in organic matters compared to inorganics,

570 leading to enhanced particle hygroscopicity and more conducive to activation.
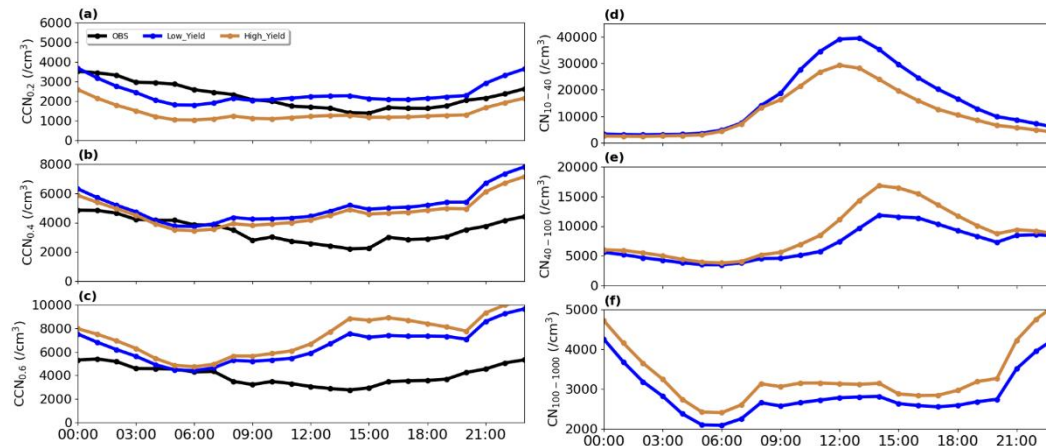
571

572 Fig. 4. Average diurnal variation of (a) $CCN_{0.2\%}$, (b) $CCN_{0.4\%}$ and (c) $CCN_{0.6\%}$ and (d)

573 CN_{10-40}, (e) CN_{40-100}, (f) $CN_{100-1000}$ on NPF days in Qingdao on February 5-24, 2017,

574 in Low_yield and High_yield simulations, shown as blue and brown lines, and black

575 lines represent observation results.

576

577 Furthermore, compared to the high yield of SI-SOA, the low SI-SOA yield results

578 in a high CCN concentration under low SS and low CCN concentration under high SS.

579 Therefore, both the underestimates of $CCN_{0.2\%}$ (mean fractional bias of -45%) and

580 overestimates of $CCN_{0.6\%}$ (mean fractional bias of 56%) mentioned above are improved,

581 with mean fractional bias of $CCN_{0.2\%}$ and $CCN_{0.6\%}$ reaching 7% and 43%, respectively

582 (Fig. 4a,c). This result suggests that the oxidation rate of S/IVOC is possibly closer to

583 the low value, which is understandable based on Wu et al. (2021b), who found that the

584 amount of O-S/IVOCs, which corresponds to a low oxidation rate, is in general much

585 larger (i.e., 20 times) than that of PAHs with a high oxidation rate.

586 In addition to the single site of Qingdao, we further explore the impact of SI-SOA

587 yield on CCN from a larger spatial coverage (Fig. 5). Consistent with the mechanism

588 revealed over Qingdao, even from a larger spatial perspective, a lower oxidation rate of

589 S/IVOC essentially enhances CCN at a lower SS (e.g., $CCN_{0.2\%}$; Fig. 5a) with the

highest increase over North China Plain area (Fig. 5a), and weakens CCN (i.e., by 10–20% over Beijing-Tianjin-Hebei) at a higher SS (Fig. 5c), particularly over the dense emission area (Fig. S12). It is worth noting that in the 2-species VBS mechanism used in our study, all S/IVOC in the inventory is calculated based on a constant emission ratio of S/IVOC to POA from all source categories (Shrivastava et al., 2011), which may miss part of S/IVOC due to different emission ratios of POA from different source (Chang et al., 2022). In addition, the simplified VBS mechanism used in our study does not take into account the multi-step oxidation of organic species, which may introduce some uncertainties. To be more specific, in the 2-species VBS mechanism, SI-SOA with effective saturation concentrations (c^*) of 10^{-2} μg m^{-3} is formed by the vapor phase oxidation of S/IVOC vapors with c^* of 10^5 μg m^{-3}, reducing volatility by 7 orders of magnitude. The process of one-step oxidation does not mean to represent a physical process, but to parameterize the mean effect of a complex process of SOA formation (Shrivastava et al., 2011). However, in the real atmosphere, the gaseous VOCs often undergo multi-generational oxidation to form SOA (Garmash et al., 2020), during which the properties and composition of SOA change substantially. For instance, by adding the formation chemistry associated with multi-generational oxidation, Zhao et al. (2020) found improved simulations of vertical aerosol profile in the Amazon free troposphere compared to the simplified VBS mechanism.
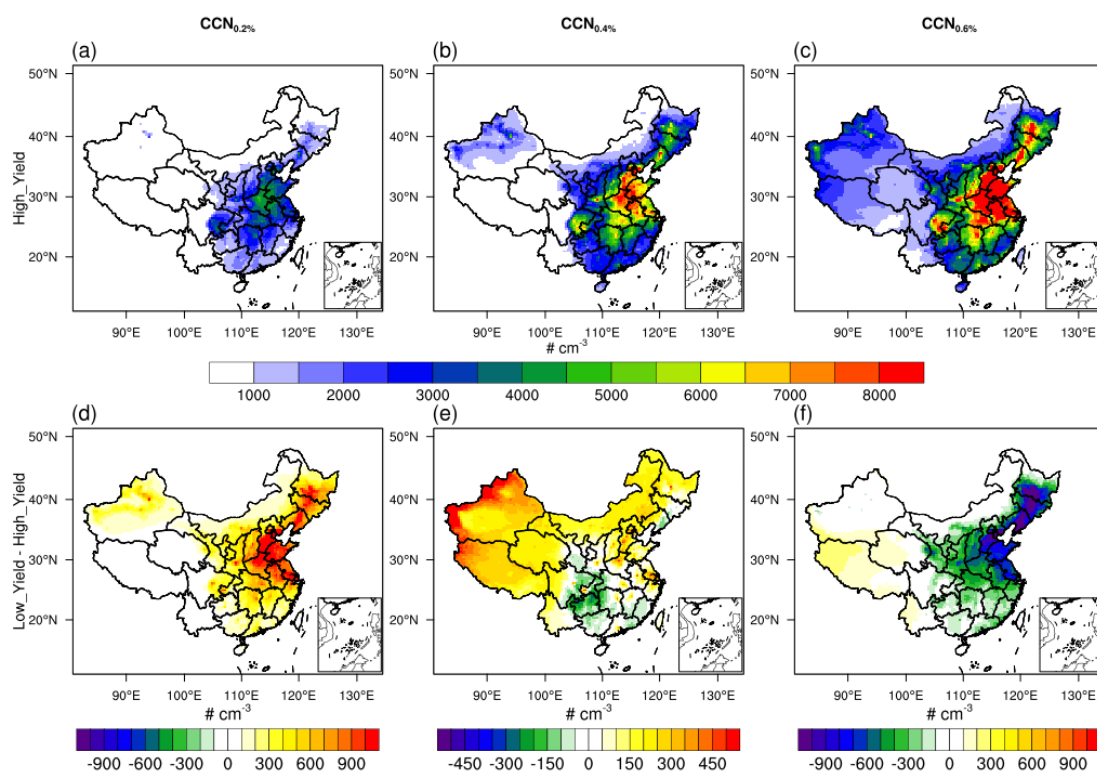
Fig. 5. Spatial distributions of CCN concentrations at different supersaturations (SS), (a) and (d) are $CCN_{0.2\%}$, (b) and (e) are $CCN_{0.4\%}$, and (c) and (f) are $CCN_{0.6\%}$. The top panels exhibit the results from the High_Yield simulation, and the bottom panels shows the difference between the Low_Yield and High_Yield simulations.
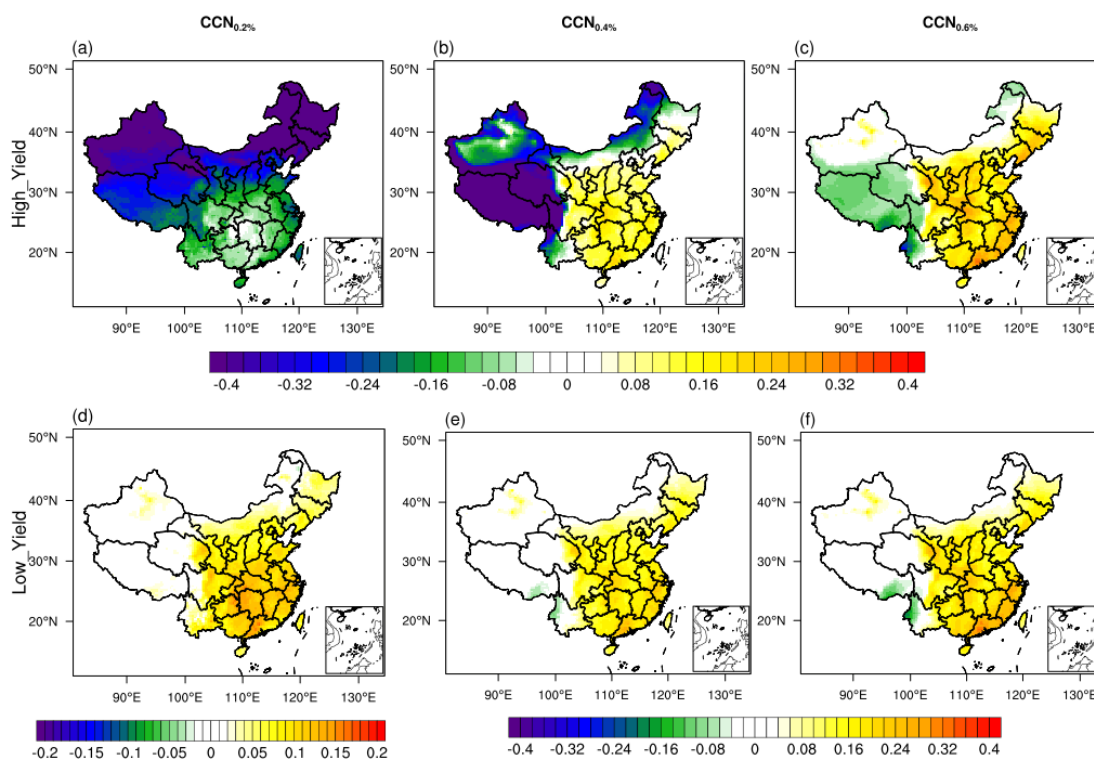
3.4 Contribution of nucleation to CCN under different SI-SOA yields

Considering the importance of nucleated particles on CCN (Yu et al., 2020; Westervelt et al., 2013), we further investigate the influence of nucleation on CCN under different SI-SOA yield conditions discussed above.

As shown in Fig. 6, in simulations close to the original model setting (High_Yield), when SS is low (i.e., SS=0.2%), the nucleation process tends to reduce the CCN by ~10–50%. In contrast, when the SS is high (0.6%), the nucleation results in a significant increase in CCN in most regions of China. When the yield of SI-SOA is adjusted to a lower level, the nucleation process has a positive contribution to CCN under both low and high SS. Especially, when SS is low (0.2%), the sign reversal, i.e., from negative (Fig. 6a) to positive (Fig. 6d) contributions of NPF to CCN along with the decrease of SI-SOA yield, i.e., the increase is concentrated in the eastern China with an average of

627 10–20%. The primary mechanism lies in that along with the decrease of SI-SOA yield,

628 the smaller fraction of SI-SOA yields an increase in hygroscopicity, which surpasses

629 the suppression effect on particle growth due to reduced SI-SOA formation. In the real

630 atmosphere, when the supersaturation is usually low, e.g. about ~0.1% in polluted areas

631 (Kalkavouras et al., 2019; Hudson and Noble, 2014), CCN will likely reduce with

632 increasing oxidation rate of S/IVOC and corresponding SI-SOA formation.

633

634

635 Fig. 6. Spatial distribution of contribution of nucleation to CCN calculated by the ratio

636 of the difference between the parameterization with and without nucleation to the

637 parameterization with nucleation under different SI-SOA yields in China in February

638 2017. (a), (d) is $CCN_{0.2\%}$, (b), (e) is $CCN_{0.4\%}$, (c), (f) is $CCN_{0.6\%}$. The upper panel and

639 lower panel represent High_Yield and Low_Yield simulation respectively

640

641 In addition to the linear-H_2SO_4 nucleation mechanism, one more empirical scheme

642 of kinetics nucleation is selected, which assumes that the nucleation rate is proportional

643 to the square of the concentration of sulfuric acid ($J = K[H_2SO_4]^2$), to investigate the

644 effect of nucleation on CCN. Substantially positive contributions of nucleation to CCN

645   is found when the low SI-SOA yield is applied, consistent with what was shown based

646   on the linear-H_2SO_4 nucleation scheme (Fig. S13). However, nucleation contributes

647   positively to CCN even when the SI-SOA yield is high in the quadratic-H_2SO_4

648   nucleation scheme (e.g., kinetics nucleation scheme). When more sulfuric acid

649   molecules participate in nucleation under this scheme than the linear-H_2SO_4 nucleation

650   scheme, the particles are more easily hygroscopically activated to CCN, which is

651   equivalent to the effect of a reduction in organic components in the linear-H_2SO_4

652   nucleation scheme (e.g., activation-type nucleation scheme). The results from this study

653   show the importance of assessing the simulated effects of the nucleation scheme on not

654   only the formation and growth process of particles but also climate factors such as CCN

655   using observations.

656

657   **Conclusions and discussions**

658   In this study, WRF-Chem explicit-NPF simulations, with linear-H_2SO_4 nucleation

659   scheme (e.g., activation-type nucleation scheme), are used to investigate the observed

660   wintertime NPF events and their contribution to CCN in China. Based on observations

661   in a typical coastal city of Qingdao, as well as in the cities of Beijing and Gucheng over

662   North China Plain, we identify high biases of the model simulated CN and CCN

663   concentrations. Therefore, we updated and improved the parameterization setting on

664   particle growth in the model, mainly including: (1) adjusting the mass accommodation

665   coefficient (α) to from the default value of 0.1 to 0.65, an important parameter for

666   sulfuric acid condensation; (2) proportionally reducing the condensation amount of

667   nitric acid on particles below 40 nm, (3) changing the emitted low-volatility POA from

668   gas to particle. Through these adjustments, the capability of the model in reproducing

669   CN and CCN is substantially improved, leading to better agreement with the observed

670   results, which significantly reduces the overestimation of CN_{10-40} (mean fractional bias

671   decreases from 48% to 1%) and CN_{40-100} (mean fractional bias decreases from 98% to

672   63%).

673

674   For CCN, due to the crucial role of SI-SOA in promoting the growth of ultrafine

675 particles, on the basis of previous studies, we lower the oxidation rate of S/IVOC and

676 hence the production rate of SI-SOA, which weakens the growth of particles to reach

677 the critical size of CCN activation, but enhances particulate hygroscopicity favoring the

678 activation to CCN. When the yield of SI-SOA is adjusted to the lower bound of

679 literature value, $CCN_{0.6\%}$ is reduced by ~10% and is closer to observations. At low SS

680 ($CCN_{0.2\%}$), the decrease of SI-SOA yield has greater effects on the increase of particle

681 hygroscopicity compared to the effect of the reduction of particle size due to the

682 decrease of condensation growth. It results in an increase of CCN (as large as ~42%) in

683 better agreement with observations. Under low SS conditions, common in the

684 atmosphere, a 2.5-fold reduction in SI-SOA yield results in a substantial increase of

685 CCN that switches from a negative contribution of new particle formation to CCN from

686 -50%~-10% to a positive contribution of 10~20%.

687   In addition to activation nucleation scheme, we have also tested a few other

688 schemes such as the quadratic-H_2SO_4 nucleation scheme (e.g., kinetics nucleation

689 scheme). Under this scheme, the bias-corrected method abovementioned is applicable

690 to improving the simulations of concentrations of CN and CCN. It is noteworthy that

691 the dependence of CCN on the SI-SOA yield is diminished, showing that under both

692 high and low yields of SI-SOA, there are positive contributions of NPF to CCN. This

693 is likely due to the increase in the amount of sulfuric acid involved in nucleation,

694 making it more hygroscopic and easier to activate to CCN, and the high content of

695 inorganic species makes them less sensitive to changes in SI-SOA yield, which deserves

696 further investigation.

697

698 **Competing interests.** At least one of the (co-)authors is a member of the editorial board

699 of Atmospheric Chemistry and Physics.

700

709 **References:**

710 Arghavani S, Rose C, Banson S, et al. 2022. The Effect of Using a New Parameterization of Nucleation
711   in the WRF-Chem Model on New Particle Formation in a Passive Volcanic Plume. Atmosphere
712   [J], 13(1): 15.

713 Buchholz R R, Emmons L K, Tilmes.S 2019. The CESM2 Development Team., 2019. CESM2.1/CAM-
714   Chem Instantaneous Output for Boundary Conditions. UCAR/NCAR - Atmospheric Chemistry
715   Observations and Modeling Laboratory.

716 Bzdek B, Zordan C, Luther G, et al. 2011. Nanoparticle Chemical Composition During New Particle
717   Formation. Aerosol Science and Technology [J], 45(1041-1048.

718 Bzdek B R, Zordan C A, Pennington M R, et al. 2012. Quantitative Assessment of the Sulfuric Acid
719   Contribution to New Particle Growth. Environmental Science & Technology [J], 46(8): 4365-
720   4373.

721 Cai C, Zhang X, Wang K, et al. 2016. Incorporation of new particle formation and early growth
722   treatments into WRF/Chem: Model improvement, evaluation, and impacts of anthropogenic
723   aerosols over East Asia. Atmospheric Environment [J], 124(262-284.

724 Cai J, Chu B, Yao L, et al. 2020. Size-segregated particle number and mass concentrations from different
725   emission sources in urban Beijing. Atmos. Chem. Phys. [J], 20(21): 12721-12740.

726 Carter W 2000. Documentation of the SAPRC-99 Chemical Mechanism for VOC Reactivity Assessment.
727   Final Report to California Air Resources Board [J].

728 Chang X, Zhao B, Zheng H, et al. 2022. Full-volatility emission framework corrects missing and
729   underestimated secondary organic aerosol sources. One Earth [J], 5(403-412.

730 Chen F, Dudhia J 2000. Coupling an Advanced Land-Surface/Hydrology Model with the Penn
731   State/NCAR MM5 Modeling System. 129(

732 Cheng Y, Su H, Koop T, et al. 2015. Size dependence of phase transitions in aerosol nanoparticles. Nature
733   Communications [J], 6(1): 5923.

734 Chrit M, Sartelet K, Sciare J, et al. 2018. Modeling organic aerosol concentrations and properties during
735   winter 2014 in the northwestern Mediterranean region. Atmos. Chem. Phys. [J], 18(24): 18079-
736   18100.

737 Chu B, Kerminen V-M, Bianchi F, et al. 2019. Atmospheric new particle formation in China.
738   Atmospheric Chemistry and Physics [J], 19(115-138.

739 Dal Maso M, Kulmala M, Riipinen I, et al. 2005. Formation and growth of fresh atmospheric aerosols:
740   Eight years of aerosol size distribution data from SMEAR II, Hyytiälä, Finland. Boreal
741   Environment Research [J], 10(323-336.

742 Davidovits P, Worsnop D R, Jayne J T, et al. 2004. Mass accommodation coefficient of water vapor on
743   liquid water. Geophysical Research Letters [J], 31(22).

744　Donahue N M, Robinson A L, Stanier C O, et al. 2006. Coupled Partitioning, Dilution, and Chemical
745　　　　Aging of Semivolatile Organics. Environmental Science & Technology [J], 40(8): 2635-2643.
746　Dong C, Matsui H, Spak S, et al. 2019. Impacts of New Particle Formation on Short-term Meteorology
747　　　　and Air Quality as Determined by the NPF-explicit WRF-Chem in the Midwestern United States.
748　　　　Aerosol and Air Quality Research [J], 19(2): 204-220.
749　Dusek U, Frank G P, Hildebrandt L, et al. 2006. Size Matters More Than Chemistry for Cloud-Nucleating
750　　　　Ability of Aerosol Particles. Science [J], 312(5778): 1375-1378.
751　Ehn M, Thornton J, Kleist E, et al. 2014. A large source of low-volatility secondary organic aerosol.
752　　　　Nature [J], 506(476-479.
753　Fanourgakis G S, Kanakidou M, Nenes A, et al. 2019. Evaluation of global simulations of aerosol particle
754　　　　and cloud condensation nuclei number, with implications for cloud droplet formation. Atmos.
755　　　　Chem. Phys. [J], 19(13): 8591-8617.
756　Gordon H, Kirkby J, Baltensperger U, et al. 2017. Causes and importance of new particle formation in
757　　　　the present-day and preindustrial atmospheres. 122(16): 8739-8760.
758　Grell G A 1993. Prognostic Evaluation of Assumptions Used by Cumulus Parameterizations. Monthly
759　　　　Weather Review [J], 121(3): 764-787.
760　Guo S, Hu M, Zamora M L, et al. 2014. Elucidating severe urban haze formation in China. Proceedings
761　　　　of the National Academy of Sciences [J], 111(49): 17373-17378.
762　Hong S-Y, Noh Y, Dudhia J 2006. A New Vertical Diffusion Package with an Explicit Treatment of
763　　　　Entrainment Processes. Monthly Weather Review - MON WEATHER REV [J], 134(
764　Hudson J G, Noble S 2014. CCN and Vertical Velocity Influences on Droplet Concentrations and
765　　　　Supersaturations in Clean and Polluted Stratus Clouds. Journal of the Atmospheric Sciences [J],
766　　　　71(1): 312-331.
767　Iacono M, Delamere J, Mlawer E, et al. 2008. Radiative Forcing by Long-Lived Greenhouse Gases:
768　　　　Calculations with the AER Radiative Transfer Models. Journal of Geophysical Research [J],
769　　　　113(
770　Jimenez J L, Canagaratna M R, Donahue N M, et al. 2009. Evolution of Organic Aerosols in the
771　　　　Atmosphere. Science [J], 326(5959): 1525-1529.
772　Kalkavouras P, Bougiatioti A, Kalivitis N, et al. 2019. Regional new particle formation as modulators of
773　　　　cloud condensation nuclei and cloud droplet number in the eastern Mediterranean. Atmos. Chem.
774　　　　Phys. [J], 19(9): 6185-6203.
775　Kerminen V-M, Chen X, Vakkari V, et al. 2018. Atmospheric new particle formation and growth: Review
776　　　　of field observations. Environmental Research Letters [J], 13(
777　Krechmer J E, Day D A, Ziemann P J, et al. 2017. Direct Measurements of Gas/Particle Partitioning and
778　　　　Mass Accommodation Coefficients in Environmental Chambers. Environ Sci Technol [J],
779　　　　51(20): 11867-11875.
780　Kulmala M, Dada L, Daellenbach K R, et al. 2021. Is reducing new particle formation a plausible solution
781　　　　to mitigate particulate air pollution in Beijing and other Chinese megacities? Faraday
782　　　　Discussions [J], 226(0): 334-347.
783　Kulmala M, L L, Lehtinen K, et al. 2004. Initial steps of aerosol growth. Atmospheric Chemistry and
784　　　　Physics [J], 4(
785　Kulmala M, Petäjä T, Ehn M, et al. 2013. Chemistry of Atmospheric Nucleation: On the Recent Advances
786　　　　on Precursor Characterization and Atmospheric Cluster Composition in Connection with
787　　　　Atmospheric New Particle Formation. Annual review of physical chemistry [J], 65(

788 Kulmala M, Petäjä T, Nieminen T, et al. 2012. Measurement of the nucleation of atmospheric aerosol
789   particles. Nature Protocols [J], 7(9): 1651-1667.
790 Lai S, Hai S, Gao Y, et al. 2022. The striking effect of vertical mixing in the planetary boundary layer on
791   new particle formation in the Yangtze River Delta. Science of The Total Environment [J],
792   829(154607.
793 Lee S-H, Gordon H, Yu H, et al. 2019. New Particle Formation in the Atmosphere: From Molecular
794   Clusters to Global Climate. Journal of Geophysical Research: Atmospheres [J], 124(
795 Li K, Zhu Y, Gao H, et al. 2015. A comparative study of cloud condensation nuclei measured between
796   non-heating and heating periods at a suburb site of Qingdao in the North China. Atmospheric
797   Environment [J], 112(40-53.
798 Li M, Liu H, Geng G, et al. 2017. Anthropogenic emission inventories in China: a review. National
799   Science Review [J], 4(6): 834-866.
800 Li X, Li Y, Cai R, et al. 2022. Insufficient Condensable Organic Vapors Lead to Slow Growth of New
801   Particles in an Urban Environment. Environmental Science & Technology [J], 56(14): 9936-
802   9946.
803 Liu H J, Zhao C S, Nekat B, et al. 2014a. Aerosol hygroscopicity derived from size-segregated chemical
804   composition and its parameterization in the North China Plain. Atmos. Chem. Phys. [J], 14(5):
805   2525-2539.
806 Liu M, Matsui H 2022. Secondary Organic Aerosol Formation Regulates Cloud Condensation Nuclei in
807   the Global Remote Troposphere. Geophysical Research Letters [J], 49(18): e2022GL100543.
808 Liu X, Zhu Y, Zheng M, et al. 2014b. Production and growth of new particles during two cruise
809   campaigns in the marginal seas of China. Atmospheric Chemistry and Physics [J], 14(
810 Liu X H, Zhu Y J, Zheng M, et al. 2014c. Production and growth of new particles during two cruise
811   campaigns in the marginal seas of China. Atmos. Chem. Phys. [J], 14(15): 7941-7951.
812 Lovejoy E R, Curtius J, Froyd K D 2004. Atmospheric ion-induced nucleation of sulfuric acid and water.
813   Journal of Geophysical Research: Atmospheres [J], 109(D8).
814 Lu H, Wang G, Guo H 2022. Ambient acidic ultrafine particles in different land-use areas in two
815   representative Chinese cities. Science of The Total Environment [J], 830(154774.
816 Lu Y, Yan C, Fu Y, et al. 2019. A proxy for atmospheric daytime gaseous sulfuric acid concentration in
817   urban Beijing. Atmos. Chem. Phys. [J], 19(3): 1971-1983.
818 Lupascu A, Easter R, Zaveri R, et al. 2015. Modeling particle nucleation and growth over northern
819   California during the 2010 CARES campaign. Atmos. Chem. Phys. [J], 15(21): 12283-12313.
820 Ma N, Zhao C, Tao J, et al. 2016. Variation of CCN activity during new particle formation events in the
821   North China Plain. Atmos. Chem. Phys. [J], 16(13): 8593-8607.
822 Matsui H, Koike M, Kondo Y, et al. 2011. Impact of new particle formation on the concentrations of
823   aerosols and cloud condensation nuclei around Beijing. Journal of Geophysical Research:
824   Atmospheres [J], 116(D19).
825 Matsui H, Koike M, Takegawa N, et al. 2013. Spatial and temporal variations of new particle formation
826   in East Asia using an NPF-explicit WRF-chem model: North-south contrast in new particle
827   formation frequency. 118(20): 11,647-611,663.
828 Merikanto J, Spracklen D V, Mann G W, et al. 2009. Impact of nucleation on global CCN. Atmos. Chem.
829   Phys. [J], 9(21): 8601-8616.
830 Mikkonen S, Romakkaniemi S, Smith J N, et al. 2011. A statistical proxy for sulphuric acid concentration.
831   Atmos. Chem. Phys. [J], 11(21): 11319-11334.

832　Morrison H, Thompson G, Tatarskii V 2009. Impact of Cloud Microphysics on the Development of
833　　　　Trailing Stratiform Precipitation in a Simulated Squall Line: Comparison of One and Two-
834　　　　Moment Schemes. Monthly Weather Review - MON WEATHER REV [J], 137(991-1007.

835　Nieminen T, Kerminen V M, Petäjä T, et al. 2018. Global analysis of continental boundary layer new
836　　　　particle formation based on long-term measurements. Atmos. Chem. Phys. [J], 18(19): 14737-
837　　　　14756.

838　Petäjä T, Mauldin I R L, Kosciuch E, et al. 2009. Sulfuric acid and OH concentrations in a boreal forest
839　　　　site. Atmos. Chem. Phys. [J], 9(19): 7435-7448.

840　Pierce J, Riipinen I, Kulmala M, et al. 2011. Quantification of the volatility of secondary organic
841　　　　compounds in ultrafine particles during nucleation events. Atmospheric Chemistry and Physics
842　　　　Discussions [J], 11(14495-14539.

843　Pöschl U, Canagaratna M, Jayne J T, et al. 1998. Mass Accommodation Coefficient of H2SO4 Vapor on
844　　　　Aqueous Sulfuric Acid Surfaces and Gaseous Diffusion Coefficient of H2SO4 in N2/H2O. The
845　　　　Journal of Physical Chemistry A [J], 102(49): 10082-10089.

846　Qiao X, Yan C, Li X, et al. 2021. Contribution of Atmospheric Oxygenated Organic Compounds to
847　　　　Particle Growth in an Urban Environment. Environmental Science & Technology [J], XXXX(

848　Ren J, Chen L, Fan T, et al. 2021. The NPF Effect on CCN Number Concentrations: A Review and Re-
849　　　　Evaluation of Observations From 35 Sites Worldwide. Geophysical Research Letters [J], 48(19):
850　　　　e2021GL095190.

851　Riipinen I, Sihto S L, Kulmala M, et al. 2007. Connections between atmospheric sulphuric acid and new
852　　　　particle formation during QUEST III–IV campaigns in Heidelberg and Hyytiälä. Atmos.
853　　　　Chem. Phys. [J], 7(8): 1899-1914.

854　Roldin P, Swietlicki E, Massling A, et al. 2011a. Aerosol ageing in an urban plume – implication for
855　　　　climate. Atmos. Chem. Phys. [J], 11(12): 5897-5915.

856　Roldin P, Swietlicki E, Schurgers G, et al. 2011b. Development and evaluation of the aerosol dynamics
857　　　　and gas phase chemistry model ADCHEM. Atmos. Chem. Phys. [J], 11(12): 5867-5896.

858　Saha S, Moorthi S, Wu X, et al. 2014. The NCEP Climate Forecast System Version 2. Journal of Climate
859　　　　[J], 27(6): 2185-2208.

860　Shen X, Sun J, Zhang X, et al. 2018. Comparison of Submicron Particles at a Rural and an Urban Site in
861　　　　the North China Plain during the December 2016 Heavy Pollution Episodes. Journal of
862　　　　Meteorological Research [J], 32(26-37.

863　Shrivastava M, Fast J, Easter R, et al. 2011. Modeling organic aerosols in a megacity: comparison of
864　　　　simple and complex representations of the volatility basis set approach. Atmospheric Chemistry
865　　　　and Physics [J], 11(6639-6662.

866　Shrivastava M K, Lane T E, Donahue N M, et al. 2008. Effects of gas particle partitioning and aging of
867　　　　primary emissions on urban and regional organic aerosol concentrations. 113(D18).

868　Sihto S L, Kulmala M, Kerminen V M, et al. 2006. Atmospheric sulphuric acid and aerosol formation:
869　　　　implications from atmospheric measurements for nucleation and early growth mechanisms.
870　　　　Atmos. Chem. Phys. [J], 6(12): 4079-4091.

871　Sihto S L, Mikkilä J, Vanhanen J, et al. 2011. Seasonal variation of CCN concentrations and aerosol
872　　　　activation properties in boreal forest. Atmos. Chem. Phys. [J], 11(24): 13269-13285.

873　Tewari M, Wang W, Dudhia J, et al. 2016. Implementation and verification of the united NOAH land
874　　　　surface model in the WRF model [M].

875 Virtanen A, Kannosto J, Kuuluvainen H, et al. 2011. Bounce behavior of freshly nucleated biogenic
876   secondary organic aerosol particles. Atmos. Chem. Phys. [J], 11(16): 8759-8766.

877 Wang D-W, Guo H, Chan C K 2014. Diffusion Sampler for Measurement of Acidic Ultrafine Particles
878   in the Atmosphere. Aerosol Science and Technology [J], 48(12): 1236-1246.

879 Wang J, Li M, Li L, et al. 2022. Particle number size distribution and new particle formation in Xiamen,
880   the coastal city of Southeast China in wintertime. Science of The Total Environment [J],
881   826(154208.

882 Wang Y, Wang Y, Song X, et al. 2023. The impact of particulate pollution control on aerosol
883   hygroscopicity and CCN activity in North China. Environmental Research Letters [J],
884   18(074028.

885 Westervelt D M, Pierce J R, Riipinen I, et al. 2013. Formation and growth of nucleated particles into
886   cloud condensation nuclei: model–measurement comparison. Atmos. Chem. Phys. [J], 13(15):
887   7645-7663.

888 Wu H, Li Z, Jiang M, et al. 2021a. Contributions of traffic emissions and new particle formation to the
889   ultrafine particle size distribution in the megacity of Beijing. Atmospheric Environment [J],
890   262(118652.

891 Wu L, Ling Z, Shao M, et al. 2021b. Roles of Semivolatile/Intermediate-Volatility Organic Compounds
892   on SOA Formation Over China During a Pollution Episode: Sensitivity Analysis and
893   Implications for Future Studies. Journal of Geophysical Research: Atmospheres [J], 126(8):
894   e2020JD033999.

895 Wu Z, Hu M, Yue D, et al. 2011. Evolution of particle number size distribution in an urban atmosphere
896   during episodes of heavy pollution and new particle formation. Science China Earth Sciences
897   [J], 54(11): 1772.

898 Yao L, Garmash O, Bianchi F, et al. 2018. Atmospheric new particle formation from sulfuric acid and
899   amines in a Chinese megacity. Science [J], 361(278-281.

900 Yu F 2005. Quasi-unary homogeneous nucleation of H2SO4-H2O. The Journal of Chemical Physics [J],
901   122(7): 074501.

902 Yu F, Luo G, Nair A A, et al. 2020. Wintertime new particle formation and its contribution to cloud
903   condensation nuclei in the Northeastern United States. Atmos. Chem. Phys. [J], 20(4): 2591-
904   2601.

905 Yu F, Luo G, Pryor S C, et al. 2015. Spring and summer contrast in new particle formation over nine
906   forest areas in North America. Atmos. Chem. Phys. [J], 15(24): 13993-14003.

907 Yuan Q, Li W, Zhou S, et al. 2015. Integrated evaluation of aerosols during haze-fog episodes at one
908   regional background site in North China Plain. Atmospheric Research [J], 156(102-110.

909 Yue D L, Hu M, Zhang R Y, et al. 2011. Potential contribution of new particle formation to cloud
910   condensation nuclei in Beijing. Atmospheric Environment [J], 45(33): 6070-6077.

911 Zaveri R A, Easter R C, Fast J D, et al. 2008. Model for Simulating Aerosol Interactions and Chemistry
912   (MOSAIC). 113(D13).

913 Zaveri R A, Easter R C, Peters L K 2005. A computationally efficient Multicomponent Equilibrium
914   Solver for Aerosols (MESA). Journal of Geophysical Research: Atmospheres [J], 110(D24).

915 Zhang Q, Jimenez J L, Canagaratna M R, et al. 2007. Ubiquity and dominance of oxygenated species in
916   organic aerosols in anthropogenically-influenced Northern Hemisphere midlatitudes.
917   Geophysical Research Letters [J], 34(13).

918   Zhao B, Shrivastava M, Donahue N M, et al. 2020. High concentration of ultrafine particles in the
919   Amazon free troposphere produced by organic new particle formation. Proceedings of the
920   National Academy of Sciences [J], 117(41): 25344-25351.

921   Zhao B, Wang S, Donahue N M, et al. 2016. Quantifying the effect of organic aerosol aging and
922   intermediate-volatility emissions on regional-scale aerosol pollution in China. Scientific
923   Reports [J], 6(1): 28815.

924   Zheng B, Tong D, Li M, et al. 2018. Trends in China's anthropogenic emissions since 2010 as the
925   consequence of clean air actions. Atmos. Chem. Phys. [J], 18(19): 14095-14111.

926   Zhu Y, Li K, Shen Y, et al. 2019. New particle formation in the marine atmosphere during seven cruise
927   campaigns. Atmos. Chem. Phys. [J], 19(1): 89-113.

928   Zhu Y, Sabaliauskas K, Liu X, et al. 2014. Comparative analysis of new particle formation events in less
929   and severely polluted urban atmosphere. Atmospheric Environment [J], 98(655-664.

930   Zhu Y, Shen Y, Li K, et al. 2021. Investigation of Particle Number Concentrations and New Particle
931   Formation With Largely Reduced Air Pollutant Emissions at a Coastal Semi-Urban Site in
932   Northern China. Journal of Geophysical Research: Atmospheres [J], 126(17): e2021JD035419.

933

934